Chasing DRAGNs: A Numerical Investigation into the Absence of Plume Structures in Observations of Double Radiosources Associated with Galactic Nuclei

by

Stephen M. Campbell

A THESIS SUBMITTED IN PARTIAL FULFILMENT OF
THE REQUIREMENTS FOR THE DEGREE OF

BACHELOR OF SCIENCE

in

Honours Astrophysics

(Department of Astronomy and Physics, Dr. David A. Clarke supervising faculty)

. . . .

. . . .

. . . .

. . . .

. . . .

SAINT MARY'S UNIVERSITY

April 22, 2014

© Stephen M. Campbell, 2014

ACKNOWLEDGEMENTS

I would like to express my sincere thanks to Dr. David Clarke, who has always made his guidance available to me during my time at Saint Mary's University, and especially so throughout the creation of this thesis. As well, to my parents, Michael and Karen, and to Regan, for without their love and support I would not have succeed in this endeavor. To these wonderful people I dedicate this thesis.

Abstract

Chasing DRAGNs: A Numerical Investigation into the Absence of

Plume Structures in Observations of Double Radiosources

Associated with Galactic Nuclei

by *Stephen M. Campbell*

submitted on April 22, 2014:

The formation of plume structures has long been a consequence of fluid modelling of extragalactic radio jets. Simulations performed to date, which have been executed with and without reflective boundary conditions along the equatorial plane, have exhibited these structures, without being able to explain their lack of prevalence in the observations.

I have shown, through use of synthetic synchrotron emission images, that plumes should indeed exist in radio observations and suggest that, because of the extremely low energy content of the material in the plumes, these structures should be visible for any source given a low enough observation frequency.

Contents

List of Figures

List of Tables

Chapter 1

INTRODUCTION

1.1 RADIO JETS

M87, a giant elliptical galaxy in Virgo, was first noted for its peculiarity by Curtis (1918), who described it as a "curious straight ray...apparently connected to the nucleus by a thin line of matter". It was later confirmed as a strong radio source by Baade & Minkowski (1954). Evident in figure 1.1 (Hines et al., 1989) is the feature noted by Curtis extending approximately $25''$ from the nucleus, now commonly referred to as a jet. At the distance of M87 (16 Mpc) this corresponds to approximately 1500 pc. Neither Curtis nor Baade & Minkowski gave any hypothesis on the formation of the jet feature nor the state of the jet material.

Further study into radio sources (Baade and Minkowski, 1954) lead to objects showing extended radio emission of low intensity in lobe structures with compact regions of high brightness embedded within them referred to as 'hot spots' (see figure 1.2). Sources showing extended lobe features were much more commonly observed at the time than those with jets like that of M87 (figure 1.1) or Cygnus A (figure 1.2).

In the 1970's, a distinction was made between two classes of radio sources (Fanaroff and Riley, 1974). Active radio sources showing decreasing luminosity as the distance
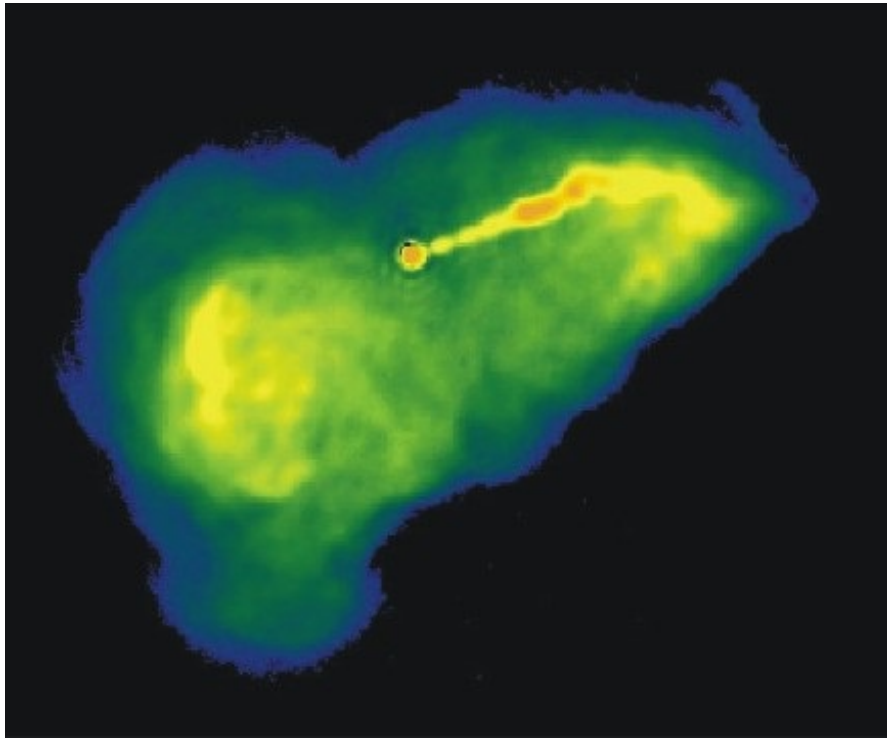
Figure 1.1: The object M87 imaged at 1.4GHz. Image courtesy of NRAO/AUI and F. Owen

from the nucleus increases (*i.e.* into the lobe structure) are said to be of class I (FR-I) (*e.g* figures 1.1 and 1.3), whereas class II (FR-II) sources show increasing luminosity in the lobes (*e.g.* figure 1.2). A clear division between the classes in the total source power at 178MHz (P_{178}) was noted at 2×10^{25} W Hz^{-1}(Fanaroff and Riley, 1974). Objects below the cut off are almost entirely FR-I, while those above are nearly all FR-II. FR-I objects are typically associated with small elliptical galaxies belonging to galxy clusters. FR-II sources, on the other hand, tend to be associated with distant quasars (precursors to the nearby galaxies, *e.g* figure 1.4) and with giant elliptical, even central dominated, galaxies closer by (figure 1.2).

As better instrumentation was developed, such as the radio telescope interferometers MERLIN (Foley and Davis, 1985) and the VLA (Hjellming, 1983), features
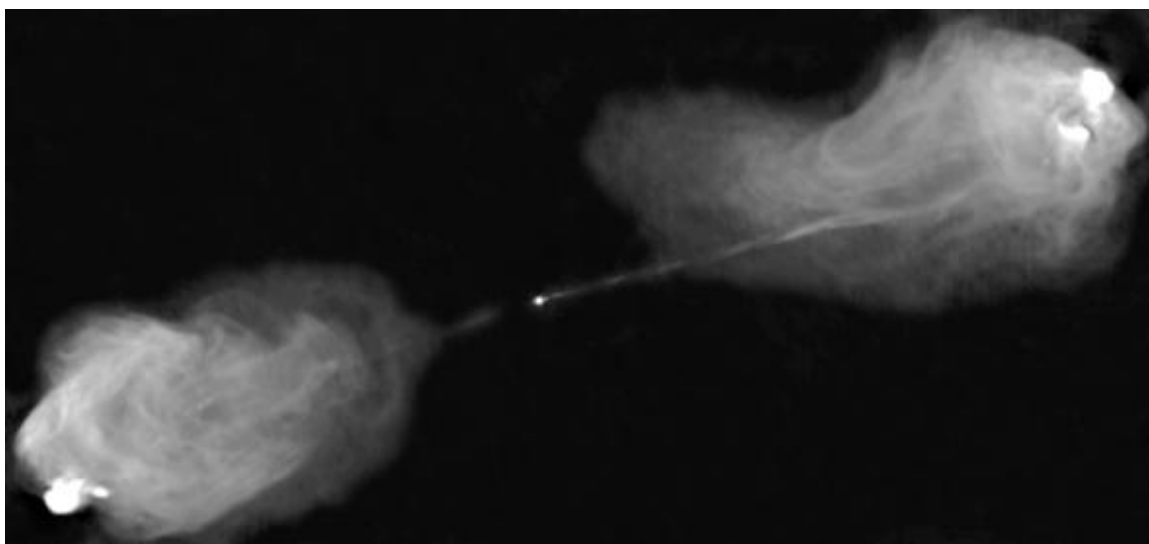
Figure 1.2: The object Cygnus A imaged at 5.0GHz. "Hotpots" are visible as the bright emission regions in the top-right and bottom-left corners. Image courtesy of NRAO/AUI, R. Perley, C. Carilli & J. Dreher

within the radio sources become resolved and many were shown to contain radio jets (Bridle and Perley, 1984). Radio jets are considered to be the mechanism of energy transport within active radio sources from the core to the lobe regions, even though many sources present observationally as double-lobes with a single jet. Investigations of jets seek to answer the remaining question of sidedness, as well as more intrinsic characteristics such as material properties, pressures, magnetic field strengths and flow velocities.

1.2 OBSERVATIONS

This investigation is a direct continuation of the work of Mike Seymour. For a more in depth perspective of the field up to the 1990's, the interested reader is referred to his thesis (Seymour, 1997).
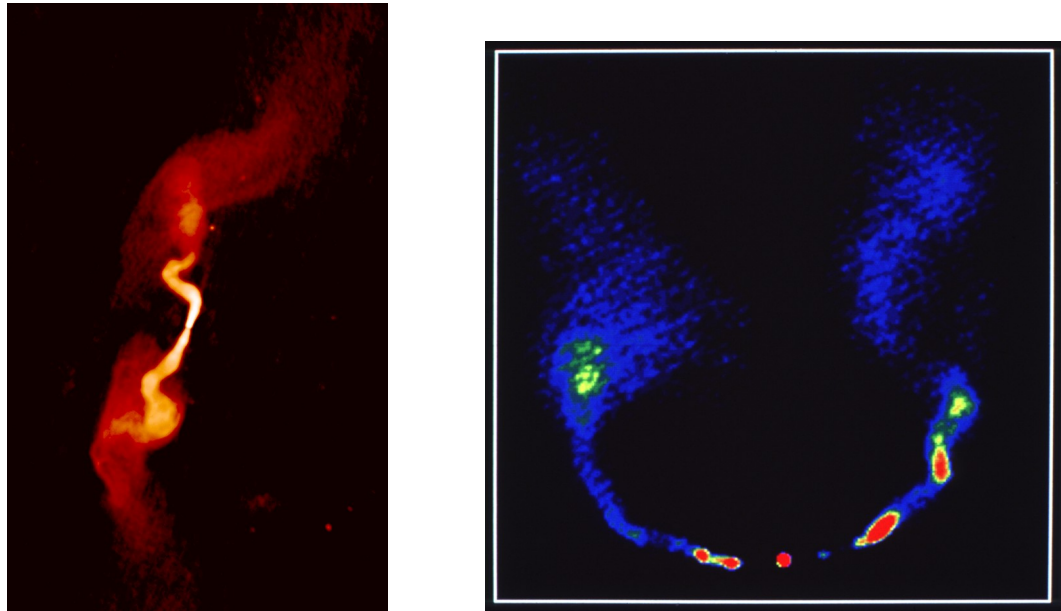
(a) 3C31 imaged at 1.4GHz showing S-shaped jets.

(b) The C-shaped jet source 3C83.1.

Figure 1.3: Exemplar images for observed jet morphologies. Images courtesy of NRAO/AUI as well as R. Laing, A. Bridle, R. Perley, L. Feretti, G. Giovannini, & P. Parma. (figure 1.3a) and C. O'Dea & F. Owen (figure 1.3b)

Weak radio sources (FR-I) tend to show two sided jets on kiloparsec scales (Bridle and Perley, 1984). These sources are often devoid of hotspots or ordered lobe features. Instead, luminous material fades out into the intergalactic medium (IGM), often forming S-shaped (figure 1.3a) or C-shaped structures (figure 1.3b) (O'Dea and Owen, 1986).

Strong radio sources (FR-II) exhibit extended lobes (see figure 1.5), with hotpot regions of higher radio intensity near the outer limits of the detected lobes. A compact core region, associated with the nucleus of a galaxy (known as an "active galactic nucleus", or AGN), is connected to the lobes by collimated jet features which are thought to be highly relativistic, though observations often show only one jet.

Some FR-II observations also show the existence of lower intensity plumes around
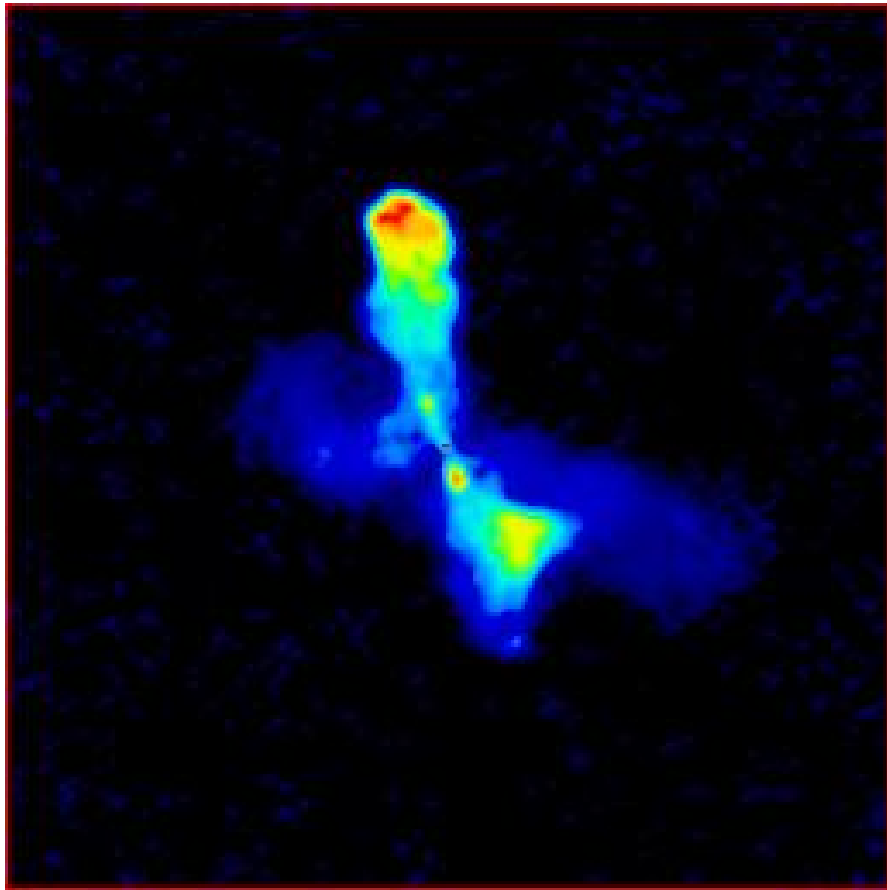
Figure 1.4: The object 4C 12.03 imaged at 1.4Ghz. Image credit Leahy and Perley, reproduced with permission.

the core. These present as extended features perpendicular to the jet axis that increase in brightness when observed at longer wavelengths (see figure 1.4).

Very Long Baseline Interferometry (VLBI) observations are used to determine apparent jet speeds by directly measuring the distance features move over several-year time periods. VLBI is used because the milliarcseond resolution (Middelberg et al., 2013) enables the imaging of small features that are not resolved with VLA. Many jets exhibit apparent superluminal motion on both parsec (Homan et al., 2001) and kiloparsec (Mullin et al., 2008) scales. This is merely a projection effect caused by orientation of the jet axis against the sky. Observed jet speeds range from $\beta_j = v_j/c \sim$
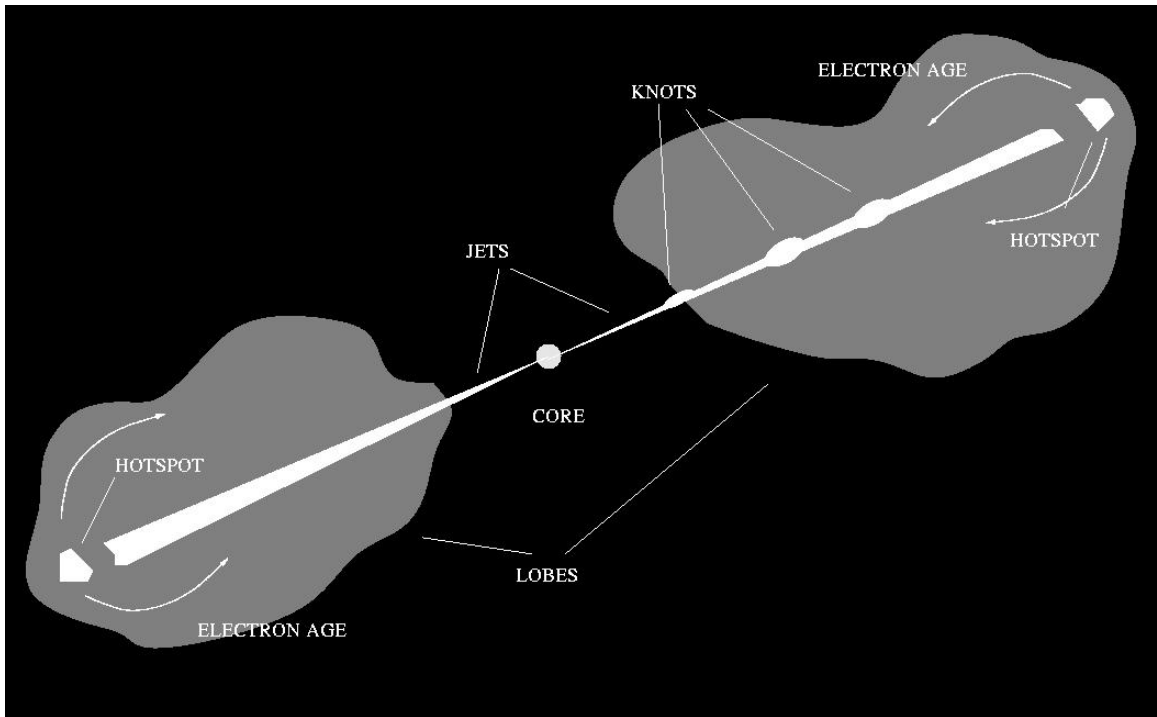
Figure 1.5: Cartoon of a double radio source. Noted features include a compact core, both radio jets, emission knots, extended lobe structures and hotspots within the lobes. The arrows indicating the direction of electron aging is addressed in section 2.2.

0.1 in Centaurus A (Tingay et al., 1998) to $\beta_j \sim 0.95$ in 3C 345 (Vermeulen, 1996).

As all extragalactic jets appear to be at least somewhat relativistic, beaming effects are considered to explain certain phenomena, most important of which being jet-sidedness. Single jet detection occurrences in strong radio sources are by far the most prevalent. If the plane of the jet is tilted at an angle with the plane of the sky the jet flowing toward the observer will be Doppler boosted, appearing brighter, while the opposite jet will be Doppler diminished, often to the point where it becomes undetectable.

The so-called Laing-Garrington effect provides further evidence for the relativistic beaming in jets (Laing, 1988; Garrington et al., 1988). The effect describes the

association between jet detected side with the less depolarized lobe. Depolarization is caused by differential Faraday rotation through irregularities in a magnetoionic medium surrounding the radio source; the jet closer to observer should be less depolarized as there is less depolarizing medium between us and the lobe (Laing, 1988). The tendency for the jet, or the brighter jet in the case of a double detection, to be associated with this lobe implies that beaming is a key factor in jet detection (Scheuer, 1987).

Another observation is that the less depolarized lobe is characterized by a flatter spectral index (Liu-Pooley correlation) (Liu and Pooley, 1991). Upon investigation this effect was correlated with jet detection, which is known to be a manifestation of Doppler beaming, suggesting that the spectral index asymmetry in the lobes is also a relativistic effect (Dennett-Thorpe et al., 1997).

The intrinsic brightness temperature of a source, $T_{b,int}$ is assumed to be associated with the equipartition temperature, T_{eq} (Readhead, 1994). T_{eq} is the calculated value of source temperature for maximum synchrotron emission lifetime assuming energy is equally divided amongst the radiative particles and the magnetic field. VLBI can be used to determine the observed brightness temperature of the source ($T_{b,obs}$). The difference between these values yields an excess that can be interpreted as the Doppler boosting factor (Readhead, 1994; Lähteenmäki et al., 1999). This method has been used to calculate Doppler boosting factors in many sources (Hovatta et al., 2009). More recent methods developed further support that the intrinsic brightness temperature is near the equipartition temperature (Hovatta et al., 2012).

Polarization data allow for the study of the magnetic field configuration present

in the radio sources, which must exist if the radiation is caused by the synchrotron mechanism. The data analysed from MOJAVE (Monitoring of Jets in Active Galactic Nuclei with VLBA experiments) suggest that the magnetic field configuration is helical, as the Faraday rotation measure is observed to change sign in transverse cuts along the jet axis (Hovatta et al., 2012).

1.3 SIMULATIONS

The initial 'standard model' for jet production, first proposed Blandford & Rees (1974) and subsequently refined after extensive numerical simulations begun by Norman et al. (1982), posits that a low density, supersonic jet penetrates into an equal pressure ambient medium of higher density. Many numerical simulations have been performed since (*e.g.* Steffen et al. 1996, Koide et al. 1996, Hooda and Wiita 1996, to name a few) in which the jet is launched into a quiescent, not necessarily uniform, gas from one of the computational domain boundaries.

Simulations of this type show a leading bow shock in front of the jet (due to the supersonic nature of the flow) that separates the quiescent ambient medium from the ambient material disturbed by the jet (Norman et al. 1982; see figure 1.6). The jet terminates at the 'working surface' (see figure 1.6), believed to be seen observationally as a hot spot (see figure 1.2). The working surface propagates forward with a velocity much lower than the flow speed along the jet because the density in the jet is significantly lower than in the ambient medium. This causes jet material to be strongly shocked, compressed, and redirected in the transverse direction, inflating

the lobe and making its way back toward the launch site (figure 1.6). The sideways and backward flowing material that inflates the surrounding region is best described as hot, rarefied, turbulent, transonic and super-Alfvénic (for weak magnetic fields) material that surrounds the jet, creating a "buffer", or "cocoon", protecting it from the influences of the ambient medium. As the cocoons of the opposing jets meet near the equatorial plane, flow is once again forced in a direction perpendicular to the jet axis, creating plumes around the launch site (*e.g.* Seymour, 1997).

The rearward flowing material establishes a shear layer across the contact discontinuity (CD) between the cocoon and the shocked ambient atmosphere. Kelvin-Helmholtz instabilities form eddies that perturb the jet flow (Norman et al., 1982) exciting oblique shocks within the jet. These shocks correspond to the knots observed in radio jets, and are responsible for the re-energization of the synchrotron emitting electrons.

The first magnetohydrodynamical (MHD) jet simulations examined the effects of a toroidal magnetic field on the dynamics and morphology of the propagating jet (Clarke et al., 1986). In the magnetically confined model, the cocoon was considerably less extensive than in the purely HD counterpart. Instead, material was captured by the toroidal magnetic field at the head of the jet, forming a "nose cone" leading the working surface.

The morphology of simulated jets is heavily dependent on the dimensionality imposed on the simulation. Simplifications such as reduced dimensionality (*e.g.* 2-D) and reflective boundary conditions along both the axis of the jet and the inflow boundary limited the degrees of freedom available.
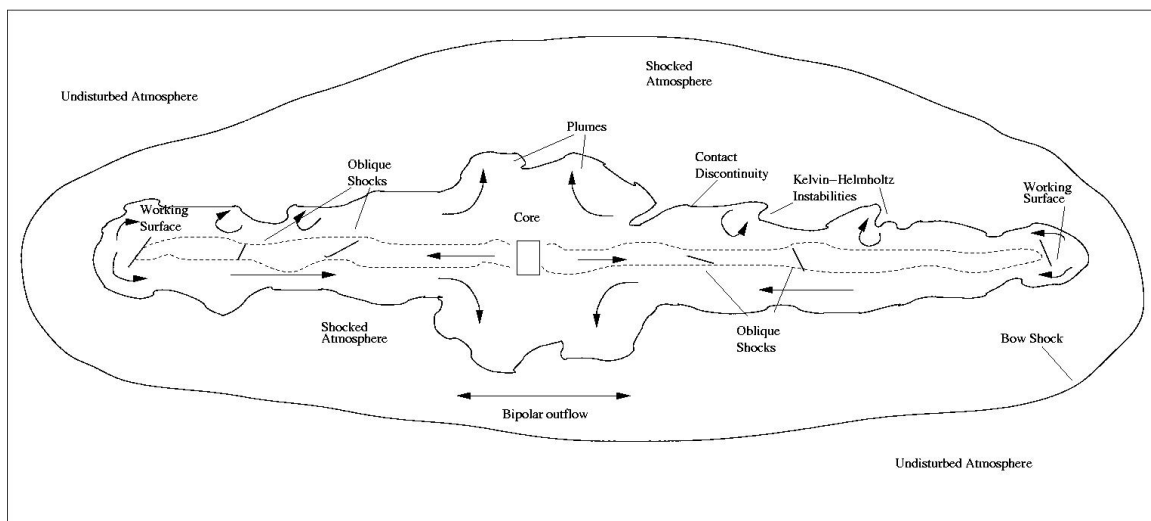
Figure 1.6: Schematic of a computer simulated double jet.

In cylindrical geometry, one is obliged to preserve top-down symmetry across the axis. In Cartesian geometry, one can "wiggle" the jet thereby breaking this symmetry and produce a more realistic simulation. The "wiggle" is created by imposing a sinusoidal velocity perturbation (one to two percent of the jet velocity) at the orifice perpendicular to the propagation direction (Norman, 1990).

Stability analysis of simulated jets showed agreement with earlier linear analysis (Hardee et al., 1991). Both 2D "slab jets" in Cartesian geometry and cylindrical jets exhibit similar spatial stability properties, and thus is was believed that the 2D "slab jet" captured the essential physics of the three-dimensional cylindrical case. It was found that jets in initial static pressure balance with the ambient medium are stabilized by adiabatic expansion and by the presence of an axial magnetic field, both of which were predicted by the linear perturbation analysis.

Initially simulations as described above were hydrodynamical (HD) in nature (*e.g.* Norman et al., 1982). Blandford & Payne (1982; hereafter, BP) posited that energy

and angular momentum were removed magnetically from accretions disks, such as those formed by growing black holes and protostars. The mechanism is such that material is driven outward along magnetic field lines protruding from the disk so long as the poloidal component of the field makes an angle of less than 60° with the disk surface. As the disk rotates, material confined by the field lines is rotated with the system. When the condition noted above is met, the rotating material is ejected outward along the field lines centrifugally, akin to a bead being flung outward on an inclined and rotating wire. At large distances the toroidal component of the magnetic field collimates the outflow into a pair of jets perpendicular to the disk surface.

Numerical work with BP type models (Ouyed and Pudritz, 1997; Ustyugova et al., 1995) supported the disk wind theory, yielding results of outflow from centrifugal effects whereby, at a point along sufficiently inclined field lines, centrifugal force dominates gravity and material is flung away. A toroidal field component is created because the field lines corotate with the disk. Inertia of the flow material forces the field to fall behind the rotation of the disk, producing the toroidal field component and, in so doing, collimates the flow and enforces the collimation far from the disk region along the length of the jet.

Meier et al. (1997) proposed the so called 'Magnetic switch' model for launching jets from AGN. The model sought to explain the speed differences noted between FR class I and II objects through different configurations of the magnetized corona of the black hole accretion disk. According to the model the flow behaviour depends on the ratio between the Alfvén velocity in the inner disk corona to the escape velocity there. A transition between transonic (FRI) and highly supersonic is induced by

increasing the magnetic field strength. The model was able to produce the required speeds and characteristic separation between the archetypes but failed to explain the morphological differences in the objects as there was no reason for the strength of the magnetic field to remain fixed at high or low values over such long timescales. (Meier, 1999).

The model was revised (Meier, 1999) to include black hole rotation as a trigger parameter within the magnetic switch. Coupled with non-Keplerian rotation in the disk, the refined model is consistent with black hole accretion models for AGN and MHD simulations of jet production while still predicting a break in the FRI/II jets speeds. The model also predicts a sharp transition in jet morphology should occur with increasing radio power, as observations show, using a mechanism — black hole spin — that allows for constant morphology over the flow time scales.

Finally, Ramsey & Clarke (2011) showed that the magnetocentrifugal launching mechanism (Blandford and Payne, 1982) is, by itself, capable of launching realistic jets on observational scales. At large distances from the disk, jet dynamics become dominated by the polodial magnetic field component, and thus, a jet launched in this way at the sub-astronomical unit (AU) scale looks, by the time it reaches the sub-pc scale to have, for all intents and purposes, been launches from a hole in the boundary. Thus, for the purposes of modelling large-scale properties of jets, the approach taken by Norman (1982) and the many others that followed is justified, and we shall assume that approach henceforth.

1.4   CURRENT INVESTIGATION

With the advent of full 3-D simulations of propagating jets, the last imposed symmetry to be dropped is the reflection symmetry implied by the boundary into which the jet is launched. Such a symmetry requires that the jet become a pair of exactly matched jets from the launch site, that there be no differences imposed by asymmetries in the ambient medium, and that the variability of the AGN be exactly identical at both poles. Observationally, this should result in every aspect, two identical jets and lobes, which is simply never observed.

When they meet up again at the equatorial plane, the back flow of two identical jets collide, redirecting back flow to a direction perpendicular to the jet axis, thus forming plumes. That plumes are so rarely observed then begs the following questions

1. Are plumes rare because asymmetric jets somehow do not form plumes as the back flow meets up? If so, what is the fate of the back flowing material?

2. Alternately, do plumes form for asymmetric jets as well but, because of observational effects, are normally absent from the observations?

Seymour (1997) was able to address the first of these questions in his 2-D HD simulations. Indeed even in strongly asymmetric jets, the back flowing material from both jets does get redirected perpendicular to the jet axis. What he was not able to address was the second question. His 2-D HD simulations did not include the magnetic fields nor did they keep track of electron age to give a good estimate of the emissivity of the flow.

This thesis addresses both of these issues. In the chapters that follow, I outline how both the magnetic field, $\vec{B}$, and the age of the emitting electrons have been added to the simulations so that it can be determined whether observational effects can account for the absence of these plumes.

Chapter 2

METHODS AND PROCEDURE

2.1   ZEUS-3D

We have opted to use the most recent version of `ZEUS-3D` (Clarke, 1996, 2010), an ideal MHD code that implements an operator-split MHD algorithm, incorporating the constrained transport (CT) method (Evans and Hawley, 1988) and the consistent method of characteristics (CMoC) (Clarke, 1996). The ideal MHD equations are as follows:

$$\frac{\partial \rho}{\partial t} + \nabla \cdot (\rho \vec{v}) = 0 \tag{2.1}$$

$$\frac{\partial \vec{s}}{\partial t} + \nabla \cdot (\vec{s}\vec{v}) = -\nabla p + \frac{1}{\mu_0}(\nabla \times \vec{B}) \times \vec{B} \tag{2.2}$$

$$\frac{\partial e_T^*}{\partial t} + \nabla \cdot (e_T^* \vec{v}) + \nabla \cdot \left(p\vec{v} + \frac{1}{\mu_0}\vec{B} \times (\vec{v} \times \vec{B}) \right) = 0 \tag{2.3}$$

$$\frac{\partial \vec{B}}{\partial t} - \nabla \times (\vec{v} \times \vec{B}) = 0 \tag{2.4}$$

$$\vec{s} = \rho \vec{v} \tag{2.5}$$

$$e_T^* = e + \frac{\rho v^2}{2} + \frac{B^2}{2\mu_0} \tag{2.6}$$

$$p = (\gamma - 1)(e_T - \frac{1}{2}\rho v^2) \tag{2.7}$$

where $\rho \equiv$ matter density, $p \equiv$ thermal pressure, $e_T^* \equiv$ total MHD energy density, $\vec{v} \equiv$ flow velocity, $\vec{s} \equiv$ momentum density, $\mu_0 \equiv$ permeability of free space and $\vec{B} \equiv$ magnetic field. These equations represent mass conservation (2.1), Newton's second law (2.2), conservation of energy (2.3) and conservation of magnetic flux (2.4) which are complemented by the constitutive equations (2.5) – (2.7).

The operator split method solves these equations in two distinct steps, the *source* step and the *transport* step. The terms on the right hand side (RHS) of equation (2.2) are updated in the *source* step, while the perfect curls and divergences in equations (2.1) – (2.4) are handled in the *transport* step.

The CT algorithm (Evans and Hawley, 1988) evolves the magnetic field while maintaining the solenoidal condition. The method uses the induced electric field, $\vec{E} = -\vec{v} \times \vec{B}$, to update the magnetic field, which is done in a way that preserves $\nabla \cdot \vec{B} = 0$ to machine round-off error within the computational domain. The CMoC algorithm is a departure from the previous MoC algorithm in that the directional-split treatment of the induction and transport operators is replaced with a planar-split scheme, required for multidimensional accuracy (Clarke, 1996). For further details on `ZEUS-3D` the interested reader is referred to Clarke (1996, 2010).

2.2 INITIALIZING A TWIN JET

In a single jet simulation, zones along the boundary are used as the jet origin (see figure 2.1) by assigning values for ρ, $\vec{v}$ and e corresponding to the conditions at the jet inlet. As the simulation progresses, these values remained unchanged while the
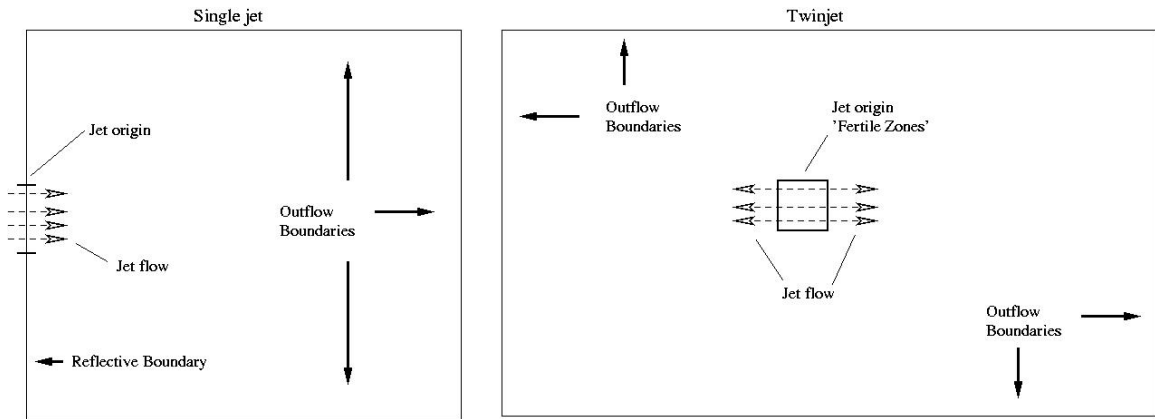
Figure 2.1: Diagram comparing the previous "single jet" to the "twinjet" computational set up. The jet inflow is moved from the domain boundary in the "single jet" scheme into the center of the domain for the "twinjet". The reflective boundary is not required, thus outflow boundaries surround the entire domain.

equations of (magneto)hydrodynamics are solved in the "active zones". This allows a supersonic jet to be launched and maintained throughout the simulation.

The "twinjet" scheme (Seymour, 1997) removes the reflective boundary condition previously used to simulate the existence of a second, or "counter" jet. This was achieved by moving the jet origin to the center of the grid (figure 2.1). In the center of the grid, a region six zones thick and as wide as the jet diameter is designated as the "fertile zone" region, in which conditions necessary to launch two opposing jets are maintained. In essence, these "fertile zones" are treated much like the boundary zones used to launch a jet in the single-jet simulations. Following each of the update steps (source and transport), the values in the "fertile zones" are overwritten with the original settings. This maintains the jet flow using a method consistent with two opposing jets launched from a compact, unresolved core region into the active grid zones.

Modifying the "fertile zones" to launch a magnetic field into the simulation proved
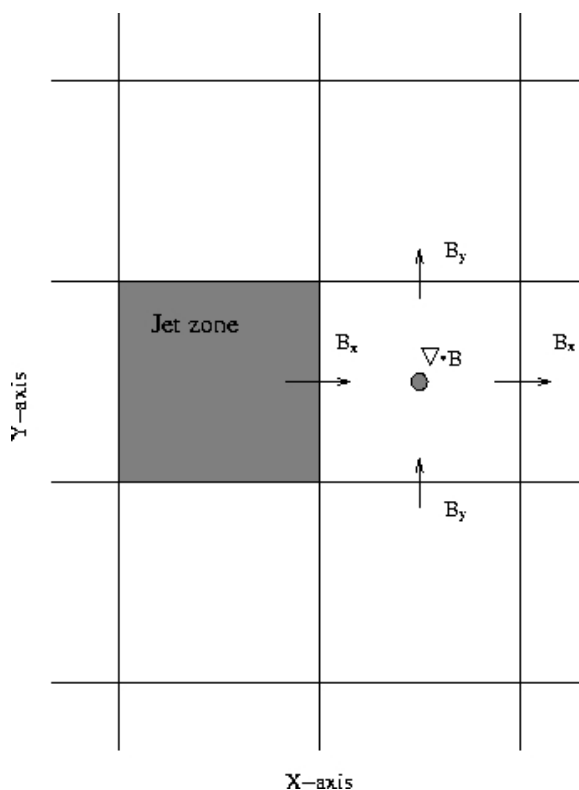
Figure 2.2: Diagram depicting basic grid scheme to update magnetic field values.

much more challenging. Consider the portion of the grid depicted in figure 2.2, showing a single "fertile zone" in grey abutting on its immediate right, an active zone on the grid. Assume that the grid is initialized in such a way that $\nabla \cdot \vec{B} = 0$ everywhere. As the jet flows onto the active grid, the magnetic field must be updated accordingly. If, after one MHD step, one were to restore the value of B_x only at the boundary interface to the value required in the jet material (as one does with the HD variables) the solenoidal condition would suddenly be violated at the zone center, labeled $\nabla \cdot \vec{B}$ in figure 2.2. In principle, this violation could be corrected by adjusting the values of B_x and B_y at the other faces of the active zone but then, by induction, it is easy to see that all values of B_i $(i = x, y, z)$ across the grid would have to be adjusted for each time step, violating the integrity of the developing MHD solution.

Instead, the magnetic field is set in the fertile zones by use of a pre-determined edge-centered vector potential which is updated in time by use of an edge-centered induced electric field. Since $\vec{E} \equiv -\vec{v} \times \vec{B}$, the induction equation may be written as:

$$\frac{\partial \vec{B}}{\partial t} + \nabla \times \vec{E} = 0.$$

Since $\vec{B} \equiv \nabla \times \vec{A}$, where $\vec{A}$ is the vector potential, this can be rewritten as:

$$\frac{\partial}{\partial t} \nabla \times \vec{A} + \nabla \times \vec{E} = \nabla \times \left(\frac{\partial \vec{A}}{\partial t} + \vec{E} \right) = 0.$$

This implies that, for the appropriate choice of gauge,

$$\frac{\partial \vec{A}}{\partial t} = -\vec{E}, \tag{2.8}$$

showing that the magnetic vector potential can be evolved with the induced electric field.

By using the vector potential, one can maintain the solenoidal condition to machine round-off error even if one alters the value of $\vec{A}$ in just one zone. To see this, first note that in the x-y plane where $\vec{A} = A_z \hat{z}$,

$$\vec{B} = \nabla \times \vec{A} = (\partial_y A_z, -\partial_x A_z, 0)$$

which implies that,

$$\nabla A_z = (\partial_x A_z, \partial_y A_z, 0) \perp \vec{B}$$

and thus contours of A_z are everywhere aligned with magnetic field lines. We can therefore imagine that A_z is to $\vec{B}$ what elevation (of a hill, for example) is to topological contours.

Thus, instead of trying to advance a particular magnetic field configuration into the grid, imagine instead the task of advancing a hill or a "bluff" of "elevation" A_z into the grid with its topographical contours being the desired magnetic field lines advancing into the grid with A_z (see figure 2.3). The problem of setting the desired $\vec{B}$ at the jet orifice then becomes a problem of setting the desired A_z (as evolved using equation 2.8) and, as Evans and Hawley (1988) and numerous others have shown, it is easy then to preserve the solenoidal condition to machine round-off.

A helical magnetic field was used for this investigation. By superposition, a toroidal field can be generated in conjunction with a poloidal field to generate a helical magnetic field configuration. It has been shown (Clarke, 1996; 2010, and references therein) that a toroidal field can be generated in a similar fashion to the poloidal field, discussed previously. By establishing $\vec{B}$ with a vector potential, $\vec{A}$, and evolving it with the induced electric field, $\vec{E}$ (as in equation 2.8), the solenoidal condition is maintained to machine round-off error. The sum of these divergence-free magnetic fields, evolved with the divergence-free induced electric field, will therefore remain divergence-free.

The `TWINJET` routine in `ZEUS-3D` uses "fertile zones" to launch the jets. Variables in these zones, which now includes the induced electric field, $\vec{E}$, which, in turn, is used to evolve $\vec{A}$, are overwritten after each update step. As $\vec{A}$ evolves in the "fertile zones" so does the magnetic field to provide the desired field configuration (*e.g.* toroidal, poloidal or even helical) transported by the jets. In this fashion, the magnetic field lines form "semi-infinite flux loops" (see figure 2.4) in which all field lines form closed loops, leaving no open field lines thereby maintaining the solenoidal condition to
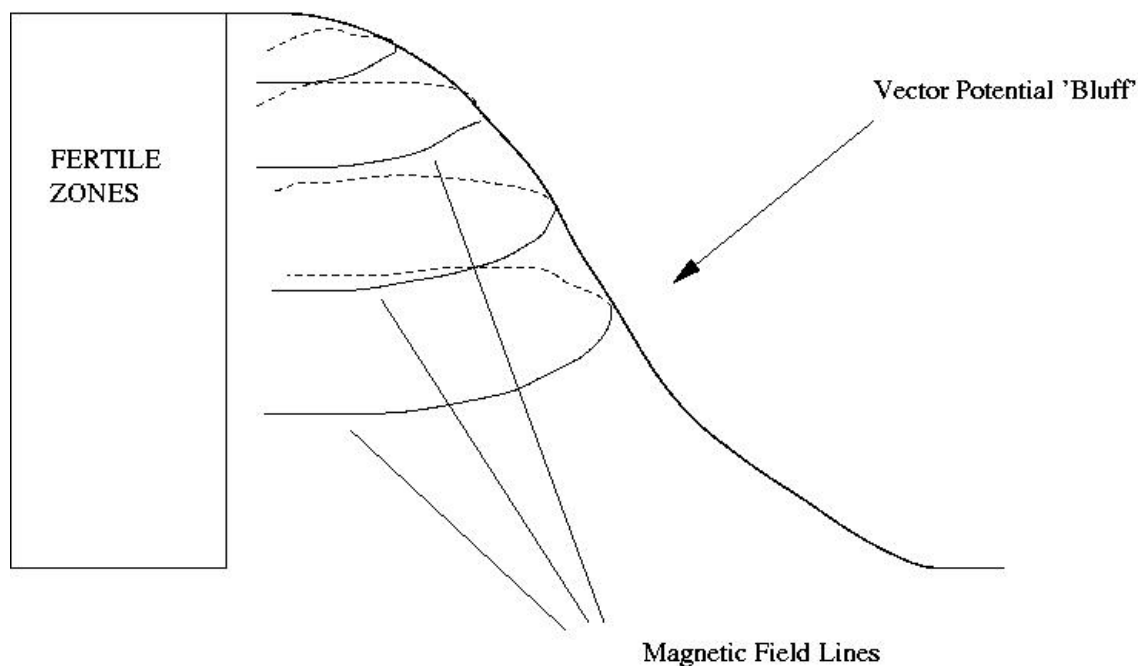
Figure 2.3: Diagram depicting the vector potential "bluff" advancing into the grid.

machine round-off everywhere.

Test simulations were executed to examine the symmetry of the "twinjet" model as well as the level of agreement between the single jet and "twinjet" schemes. All test simulations were configured in two dimensional slab symmetry, with 5 jet radii (r_j) per jet resolved in the 1-direction, and $5r_j$ in the 2-direction. The simulations were 50×50 zones for the "single jet" and 100×50 zones for the "twinjet" to maintain symmetric conditions between the schemes. The "single jet" orifice was offset by three zones into the computational grid to mimic the right half of the "fertile zones" of the "twin jet".

The "twinjet" showed agreement in the flow variables (*e.g.* ρ, $\vec{v}$) to machine round-off error between the opposing jets (see figure 2.5). The density and velocity were identical across the midplane, with an expected sign change of the axial velocity

Figure 2.4: 2-D slice of the computational domain for a small test run. The pressure of the jet is plotted (colour contours) with the magnetic field lines over-plotted (as the curl of the 3-component of the vector potential $\vec{A}$, corresponding to A_z).

(v_x) in the two jets.

The comparator simulations of the single jet launched from an offset position and the "twinjet" right propagating jet produced morphologically similar jets (see figure 2.6). Agreement between them was about one part in 10^6 (in certain tracked scalars) and not to machine round-off. It was found that the single jet is initialized with an identical x-direction velocity to the edge of the last boundary zone, while the "fertile zones" in the "twinjet" is forced the change sign at the midpoint for the "counter" jet. This difference in configuration caused differing interpolations across the base of the offset (where $v_j > 0$) and at the analogous location across the "fertile zones" (where $v_j = 0$ or < 0). These differing interpolations made their effects felt on to the active grid, causing minute differences in the single and "twinjet" simulations. These differences were very slight, and deemed to be inconsequential.
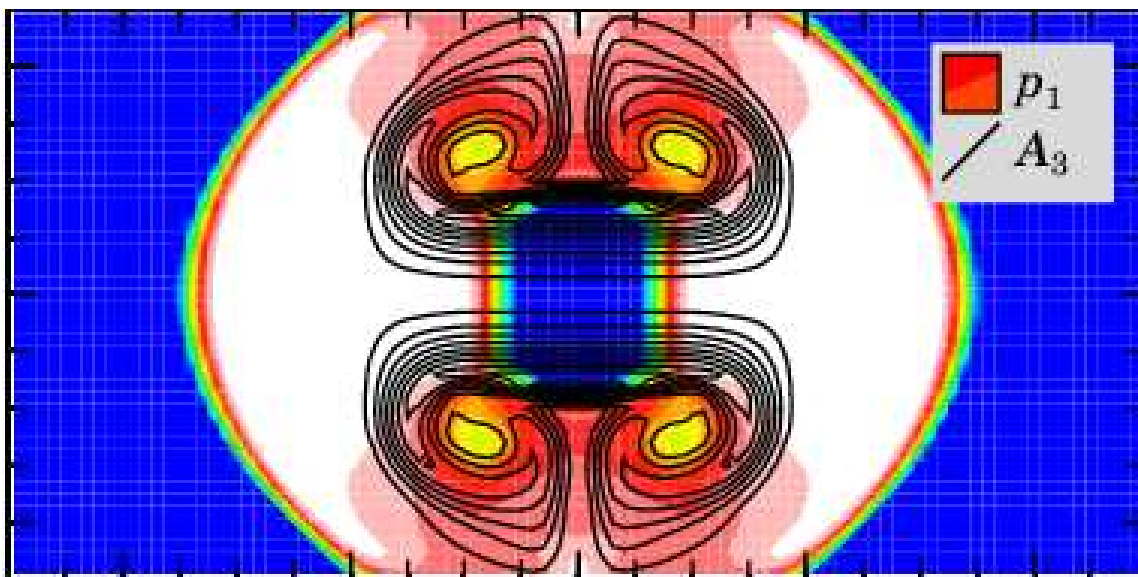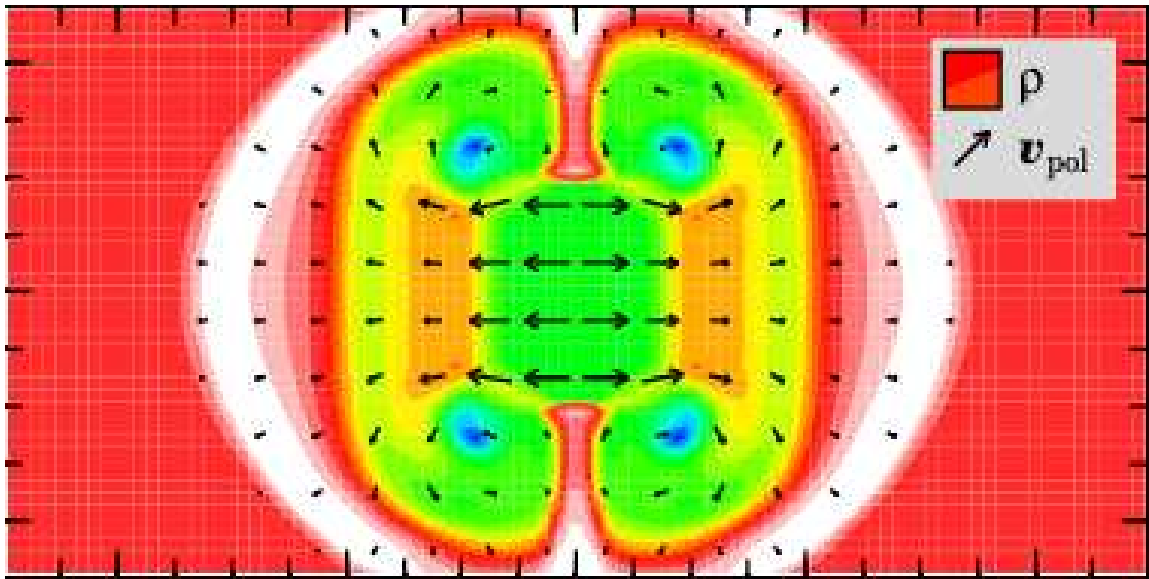
Figure 2.5: 2-D slice of the computational domain for a small test run. The density of the jet is plotted (colour contours) with the velocity vectors over-plotted.

(a) Single Jet.

(b) "Twinjet" (Right propagating)

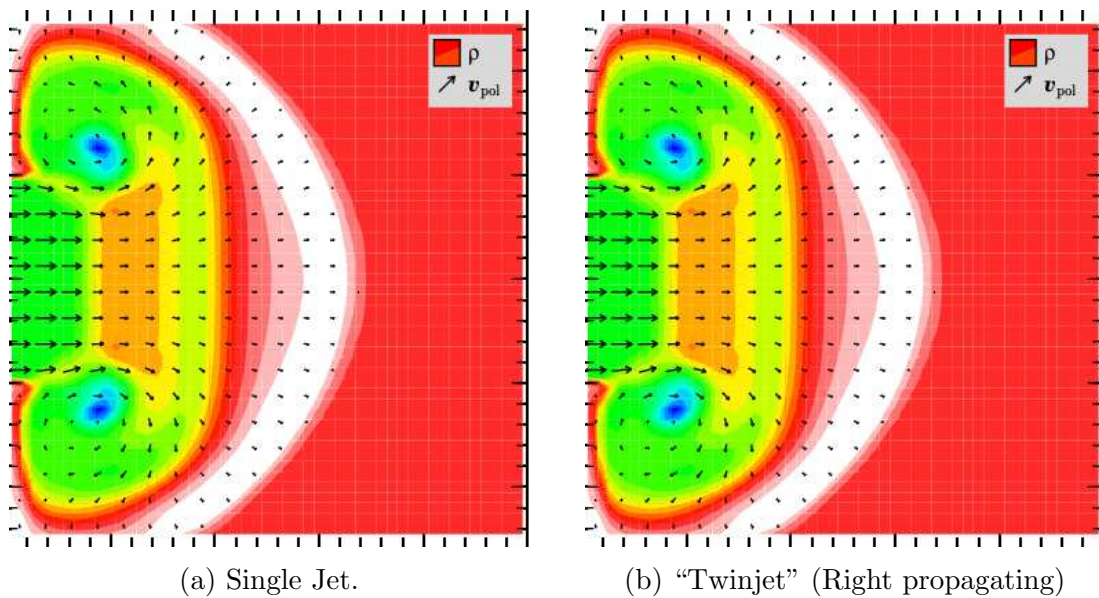Figure 2.6: 2-D slices of the computational domains for small test runs. The single jet is plotted with the "twinjet" (right propagating) for comparison. The density of the jets are plotted (colour contours) with the velocity vectors over-plotted.

The magnetic field is included in these simulations largely so that a false synchrotron emission image of the jets may be made to compare with observations. Synchrotron emission is caused by charged particles, such as electrons, spiralling about a magnetic field and, for most extragalactic radio sources obey a power-law spectrum:

$$i(\nu) \propto \nu^{-\alpha}, \tag{2.9}$$

where α is referred to as the spectral index and $i(\nu)$ is the synchrotron emissivity.

An ensemble of electrons emitting synchrotron radiation loses energy over time. To characterise this, one can define a break frequency, ν_{br}, such that for frequencies below ν_{br}, the electrons are still energetic enough to emit the full (*flatter*) synchrotron spectrum. Above ν_{br}, the electrons are depleted of energy and emit a *steeper* spectrum. For an in-depth development of the theory behind this emission model, the interested reader is referred to MacDonald (2008). Here, I will assume the results of that analysis, namely that the synchrotron age of the electron ensemble is given as:

$$t_{\mathrm{syn}} = 1.2974 \times 10^6 \ \nu_{br}^{-\frac{1}{2}} \ B^{-\frac{2}{3}}, \tag{2.10}$$

where t_{syn} is the synchrotron age of the electrons (s), ν_{br} is the break frequency of the ensemble (Hz) and B is the magnetic field strength (T). From equation 2.10, the break frequency is given by:

$$\nu_{\mathrm{br}} = 1.6761 \times 10^{12} \ B^{-3} t_{\mathrm{syn}}^{-2}. \tag{2.11}$$

The electron aging algorithm used in the simulations was developed by Nick Mac-Donald (2008). The method tracks the synchrotron age of the fluid, t_{syn} according to the following advection equation:

$$\frac{dt_{\text{syn}}}{dt} = \frac{\partial t_{\text{syn}}}{\partial t} + \vec{v} \cdot \nabla t_{\text{syn}} = 1 - \xi t_{syn} \tag{2.12}$$

where the first term on the right hand side of equation 2.12 account for synchrotron aging and the second term for shock re-acceleration. As the synchrotron age of the fluid increases, the break frequency, ν_{br}, is driven to lower frequencies. On the other hand, the synchrotron age can be reduced by shocks, effectively moving ν_{br} to higher frequencies.

With these results, the emissivity as a function of t_{syn} may be written as:

$$i(\nu, t_{\text{syn}}) = \begin{cases} \kappa_{\text{new}} (B \sin \psi)^{(x+1)/2} \, \nu^{-(x-1)/2}, & \nu < \nu_{\text{br}}; \\ \kappa_{\text{old}} (B \sin \psi)^{-2} \, \nu^{-(2x+1)/3} \, t_{\text{syn}}^{-(x+5)/3}, & \nu > \nu_{\text{br}}, \end{cases} \tag{2.13}$$

where B is the magnitude of the magnetic field, x is a power-law index related to the spectral index, α, κ_{new} and κ_{old} are proportionality constants related to the total number density of relativistic electrons contained within each portion of the spectrum, and ψ is the angle between the magnetic field and the line-of-sight. The emissivity is tracked for each zone during the calculation. The emission can be integrated along the line of sight to produce simulated synchrotron emission images that can, in principle, be compared directly to observations such as those in figures $1.2 - 1.4$.

2.3   PROCEDURE

A set of 3-D calculations were carried out using `ZEUS-3D`, with the augmented "twin-jet" scheme described previously. The jet radius (r_j) was resolved on the computational grid $(250 \times 130 \times 130$ zones) by 10 zones. Densities and Mach numbers for each jet in the various runs are listed in table 2.1. A slight precession of each jet, 180° out of phase with each other, was introduced to break the quadrantal symmetry of the calculation. The simulations were run until problem time $t = 5.0 \; r_j/c_a$ where c_a is the ambient sound speed, at which point the fastest bow shock reached the edge of the grid. The ACEnet Mahone cluster housed at Saint Mary's University was used for the production runs. Since the parallelisability of the code was not re-established and tested for this work, all runs were executed in serial, limiting the resolution of the simulations. Still, the simulations were of sufficient quality that the primary questions posed in §1.4 could be addressed.

Table 2.1: Parameters used for production runs, where the subscripts denote the left (l) or right (r) propagating jet, M is the mach number, η is the ratio of jet density to the ambient medium.

Simulation	M_l	M_r	η_l	η_r
A	10	10	0.4	0.4
B	10	10	0.2	0.2
C	9	10	0.4	0.4
D	9	10	0.2	0.2
E	9	10	0.4	0.2

Each simulation took $\sim$3 days to run on a single 2.5GHz processor. Outflow boundaries were implemented along the entirety of the computational domain. Data

were visualized using pixel dumps, 2-D slices through the computational grid, each displaying a certain variable (*e.g.* p, ρ, and emissivity, i to name a few). For the total intensity, "numerical observations" were performed at various "frequencies" (in terms of the average break frequency, ν_{br}, in the simulations which, for real extragalactic sources, typically corresponds to $\sim$5 GHz), and these results were then compared with actual observations to address the prevalence of the radio plumes.

Chapter 3

RESULTS AND DISCUSSION

3.1 NUMERICAL RESULTS

All calculations show both jets exhibiting the characteristics of the "twinjet" model as noted by Seymour (1997) (see figures 3.1 – 3.4). In each case, the jets propagate in their respective directions, terminating at a working surface. Cocoons of material are inflated around the jets which flow back into that of the opposing jet, creating plumes near the jet origin. A contact discontinuity is formed where the cocoon and plume material meets the shocked atmosphere. Kelvin-Helmholtz instabilities develop along the CD around the cocoons, most noticeable in the higher η simulations (figures 3.1 and 3.2). Bow shocks created at the leading edge of the working surface meet above and below the jet origin, forming a complete shell.
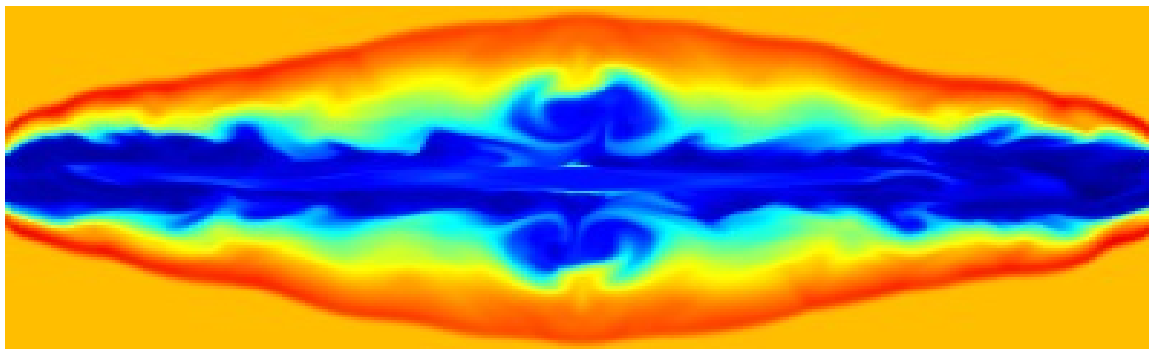

Figure 3.1: Density slice through the midplane of the computational grid for simulation A (table 2.1). High/low density regions are plotted in red/blue.

Figure 3.2: Density slice through the midplane of the computational grid for simulation D (table 2.1). High/low density regions are plotted in red/blue.

The jets launched with different opposing velocities (figures 3.2 – 3.4) show one working surface (right side) propagating faster than the other. This causes a reduced cocoon length and an inequality in the average cross sections along the length, as compared to the companion jet. As noted by Seymour (1997), the effect is caused by the rate of material flowing back from each working surface. Material flows back from the right working surface with greater velocity than the left, ultimately causing a ram-pressure imbalance near the jet origin. The cocoon material from the fast (right) jet pushes past the jet origin into the left cocoon. This causes a simultaneous deflation of the right cocoon and inflation of the left. Seymour concluded that the faster jet produces a longer and narrower cocoon than it would if the left jet were of the same power.

Mach 10 jets (those on the right side of the simulations) all advance approximately the same distance during the simulation time. In the frame of reference of the working surface, the momentum flux of the jet fluid impinging into the working surface is balanced with the momentum flux of the ambient medium pushing back against the working surface (see figure 3.5). From this, an expression for the advance speed of
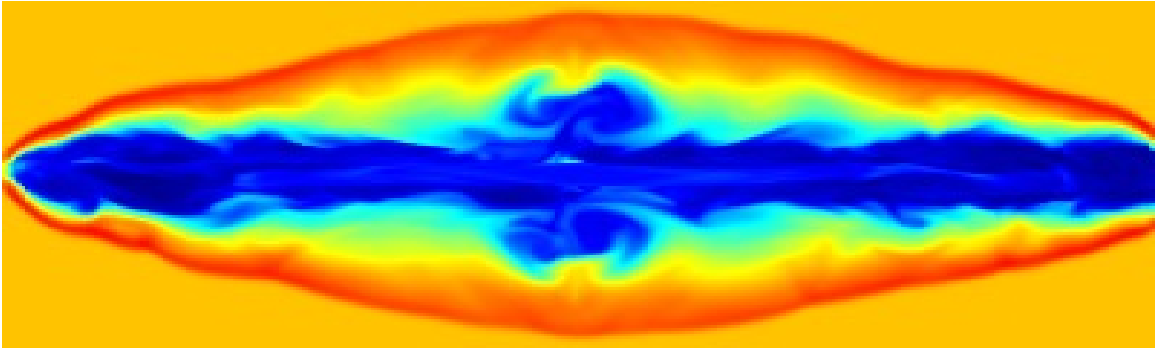
Figure 3.3: Density slice through the midplane of the computational grid for simulation C (table 2.1). High/low density regions are plotted in red/blue.
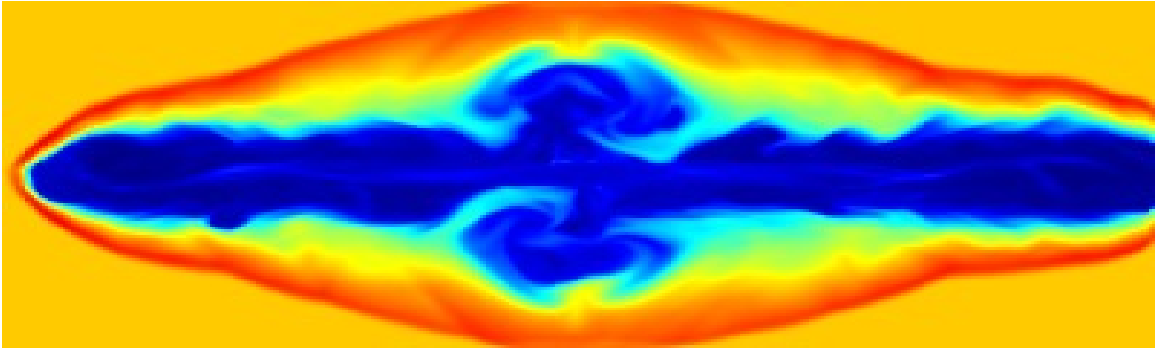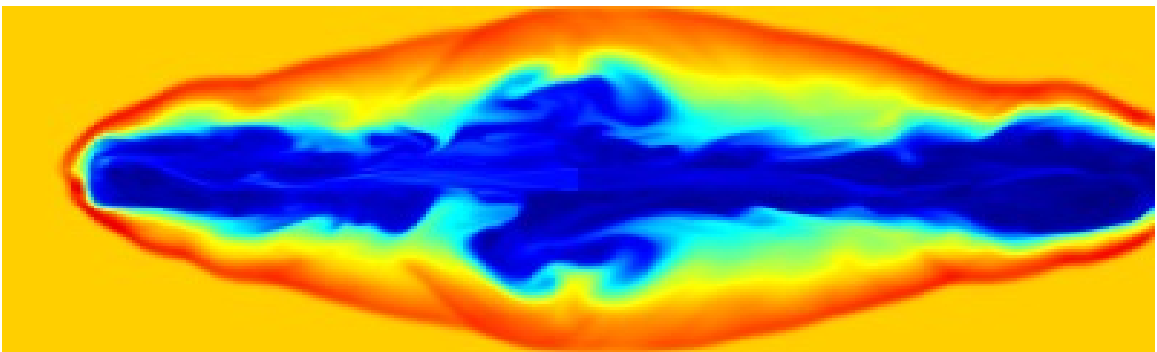

Figure 3.4: Density slice through the midplane of the computational grid for simulation E (table 2.1). High/low density regions are plotted in red/blue.
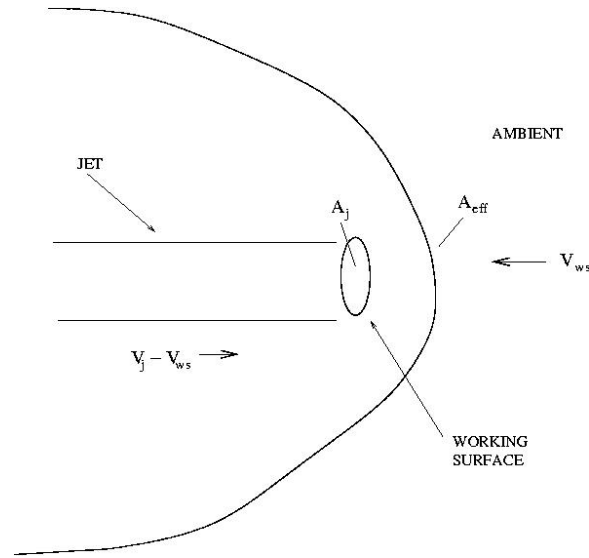
Figure 3.5: Simplified scheme of a jet in the rest frame of the working surface.

the working surface is derived as follows:

$$\rho_{\text{j}}(v_{\text{j}} - v_{\text{ws}})^2 A_{\text{j}} = \rho_{\text{amb}} v_{\text{ws}}^2 A_{\text{eff}},$$

where ρ_{j} is the jet density, ρ_{amb} is the ambient density, v_{j} is the jet velocity, v_{ws} is the velocity of the working surface, A_{j} is the area of the jet and A_{eff} is the effective area of the ambient medium as it pushes against the bow shock. Rearranging the expression in terms of v_{ws} we get:

$$v_{\text{ws}} = \frac{v_{\text{j}}}{1 + \sqrt{\frac{\varsigma}{\eta}}} = \frac{M_{\text{j}}/\sqrt{\eta}}{1 + \sqrt{\frac{\varsigma}{\eta}}} = \frac{M_{\text{j}}}{\sqrt{\eta} + \sqrt{\varsigma}},$$

where M_{j} is the Mach number of the jet, $\eta \equiv \frac{\rho_{\text{j}}}{v_{\text{amb}}}$ and $\zeta \equiv \frac{A_{\text{eff}}}{A_{\text{j}}}$. From this expression it is noted that the advance speed of the working surface has a very weak dependence on the value of η when $\eta << 0$ and $\zeta \sim 1$, explaining why a lower density jet of the same Mach number advances to the same approximate point during the simulation time.

Jets with a value of $\eta = 0.04$ are a little more ballistic in nature than those of

$\eta = 0.02$. As the denser jet material slams into the working surface, it moves the working surface farther into the grid than a less dense jet would and less material is forced back along the cocoon. In the lower density case ($\eta = 0.02$), the jet momentum transfer to the working surface is less, causing more back flow towards the jet origin. Thus the cocoon of the lower density tend to be hotter and have a greater diameter than those of the higher density jets. When the cocoons of the lighter jets meet and form the plumes, more material is available, inflating it to a greater size. To wit, simulations with $\eta = 0.02$ for at least one jet (figures 3.3 and 3.4) exhibit larger plumes than those with $\eta = 0.04$.

As jet material moves through the grid in both space and time, the electron age increases (see figure 3.6). Shocks along the jet reduced the electron age of the material, the last instance of which is when the material meets the working surface. From there the back flow steadily ages along the cocoon and into the plumes. Because of the reduced age, material in the cocoons and plumes is less emissive via the synchrotron mechanism than that in the jet or at the working surface. Shocked atmosphere shows the oldest electrons, pale in comparison to that of the jet or even the plume.

The electron age (equation 2.10) outlined in §2.2 was tracked throughout the grid in all simulations. From this, synthetic emission images for the simulations was created (see figure 3.7). The average break frequency, ν_{br}, (see bottom of figure 3.6) of the simulation was determined in the scale-free units of the simulation and then associated with 5.0 GHz (6cm), a typical break frequency in an extragalctic radio source. Each emission image was then created at frequencies that were multiples of ν_{br}. Thus, the lowest frequency (top panel, figure 3.7) is $\frac{1}{9}$ ν_{br} (corresponding
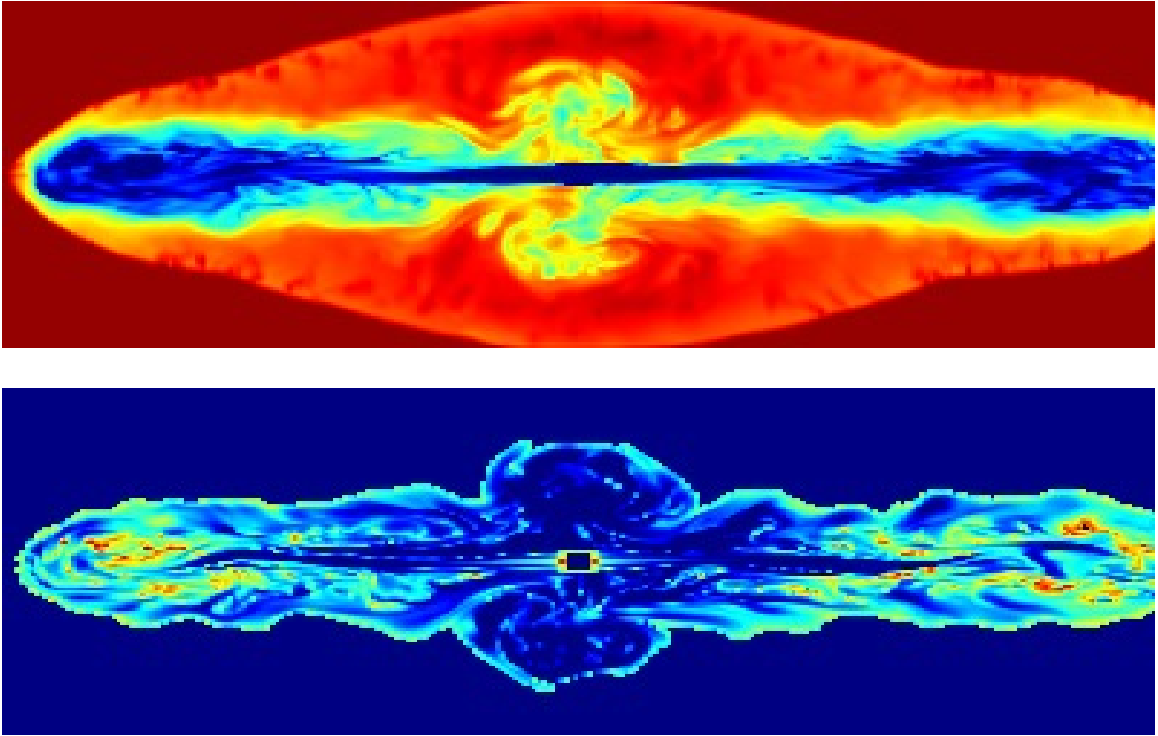
Figure 3.6: Slice through the midplane of the computational grid of electron age (top) and break frequency, ν_{br} (bottom), for simulation C. Young/old age regions are plotted in blue/red. High/low break frequency regions are plotted in red/blue.

to ∼60cm), followed by $\frac{1}{3}$ ν_{br} (second panel, ∼20cm), ν_{br} (third panel, ∼6cm) and 3 ν_{br} (bottom panel, ∼2cm). In higher observation wavelengths, increased levels of emission are evident around the "fertile zone" region, along the jet and into the the inflated cocoon towards the working surface. Whisps of emission are seen in the area corresponding to the plumes. Observationally, this would be likened to figure 1.4, exhibiting large amount of emission in the lobe regions, and dimmer, but still visible, emission in the plumes, formed from the back flow.

As the wavelength decreases, (middle), no plume emission is observed and only the brightest parts of the cocoon remain visible, corresponding to an extragalactic source more akin to Cygnus A (figure 1.2). At the shortest wavelength (bottom),

only the very edges of the jet origin and the tips of the cocoon are visible.

3.2   DISCUSSION AND CONCLUSIONS

While most extragalactic jet observations exhibit bright lobe and core emission, often times with only a single jet (figure 1.2), observations of plume structures (figure 1.4) are more rare. This thesis sought to explain these two types of observations by expanding on the "twinjet" scheme (Seymour, 1997) implemented in the magnetohydrodynamical evolution code, `ZEUS-3D`.

Multiple simulations at low resolution were executed to simulate fully 3-D, twin extragalactic jets evolved with a weak magnetic field along with a scalar to track electron age for the purposes of creating synthetic synchrotron images. Similarities and differences were observed between the synchrotron slices in figure 3.7, and the observations of actual extragalactic radio sources, as shown in figures 1.1, 1.2, 1.3a, 1.3b and 1.4.

There is a likely connection between plume detection and wavelength of observation. Often, observations exhibiting plumes are higher redshift, younger objects such as the quasars 3C 20, 4C 12.03(figure 1.4) (Leahy and Perley, 1991) and 3C 20 (R. A. Laing, unpublished) than older, more close-by objects, such as Cygnus A (figure 1.2). In the case of quasars, the rest frame wavelength of the observation would be shorter, thus visible plume structures at a longer wavelength, say 20cm, suggests that here, the electron population in the plumes remains highly energetic, much more so than in the closer radio galaxies which rarely exhibit any plumes. If the explanation
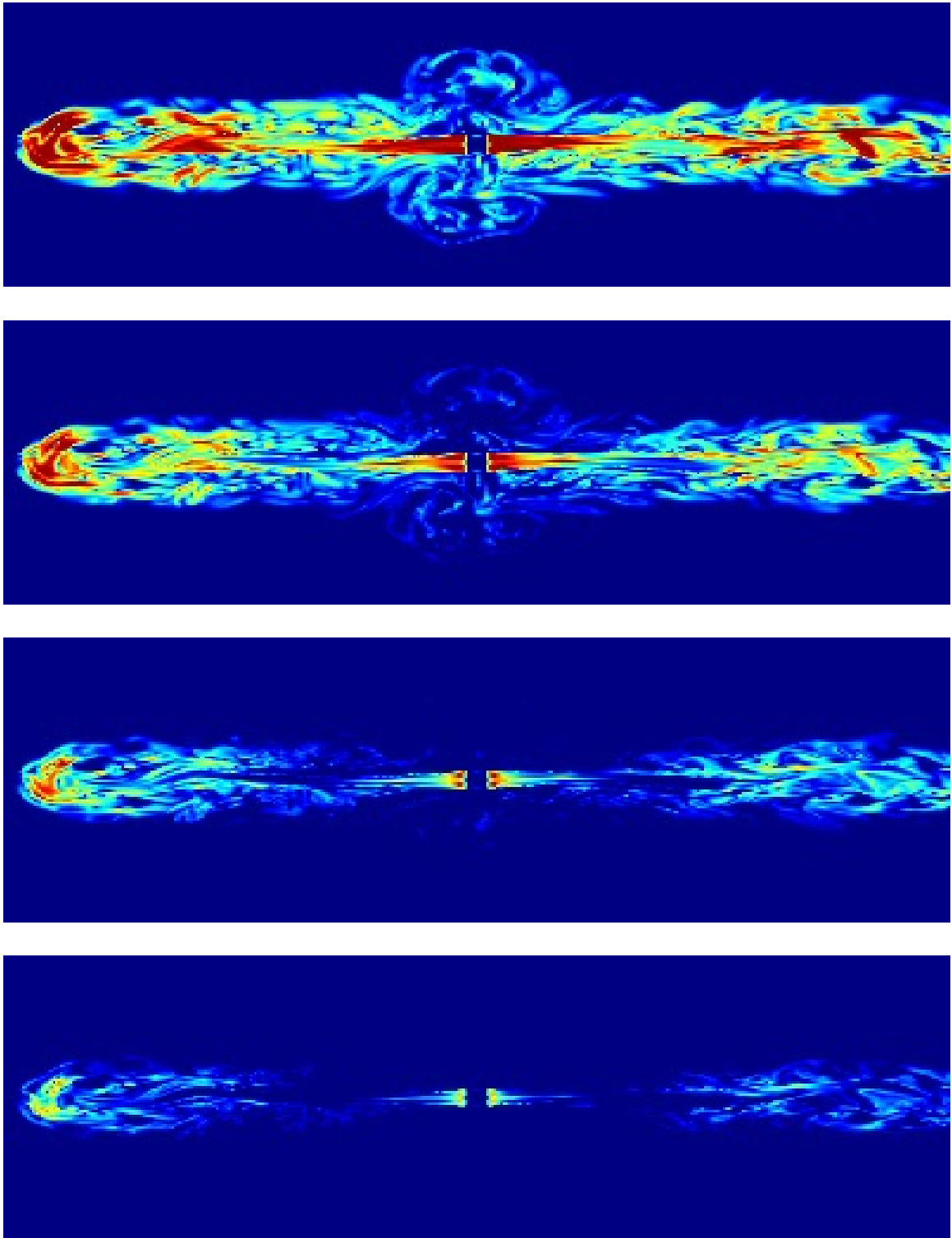
Figure 3.7: Slice through the midplane of the computational grid of the synchrotron emissivity simulation C. Images show emission at $\frac{1}{9}$, $\frac{1}{3}$, 1 and 3 times the putative average break frequency (top to bottom) set here to be 5.0 GHz. High/low emissivity is plotted in red/blue.

presented in this these for the lack of plume emission — tired electrons in the plume — this apparent counter example must be explained.

High redshift objects evolved in a younger universe, a universe in which forming AGN would have had more material in their local environments to accreate; leading to more energetic, even denser jets. Further, the higher redshift IGM is much denser than in the present epoch, providing much more resistance to the quasar jet outflow. Thus, quasar jets should be shorter and more energetic than in radio galaxies, with greater rejuvenation at the hotspots owing to the higher-density IGM. All this speaks to a plausibility argument that by the time the electrons reach the plume region in a quasar, they should be substantially more energetic than in their radio galaxy counterparts.

Absence of plume structures in observations, such as Cygnus A (figure 1.2) is likely also linked to redshift and epoch effects. In contrast to the material rich environment postulated for the plume observations, objects close to the observer would have evolved into a much sparser IGM leading to higher η, and thus more confined plume and lobe structures. Coupled with the lack of material available to the AGN, it is likely that fewer synchrotron emitting electrons would be continuously fed into the lobe structures, causing reduced emission in the back flow, and absence of plume detection.

It is therefore the conclusion of this thesis that while plumes seem to be a necessary consequence of modelling twin jets as weak-field plasma, their detection is rare largely because of observational effects. Electrons spiraling about the background magnetic field lose their energy and, as such, their ability to radiate at higher frequencies. Given

the fluid model, the oldest electrons will be in the plumes and thus, it is here that emissivity should be weakest. Compounding this could be ambipolar diffusion which, because of the presence of some neutral particles particularily those mixed in from the ambient medium along the contact, would diminish the background magnetic field strength in the oldest and most mixed portion of the backflow, namely the plumes. A prediction of this model is, therefore, that virtually all twin radio galaxies (FR-II) should exhibit plume structures if observed at a low enough frequency.

These simulations present a more complete model of twin extragalactic jets than those performed previously. Shortcomings of the work include the low resolution of the simluations and the minimal investigation of the full parameter space. Ideally, simulations that resolve the jet diameter with a minimum 40 zones should be run. The currently available resources did not permit such simulations for this work. Exploring the effect of larger asymmetries between the two jets can and should be attempted. Lower values of η representing more a physically realistic problem, and a density gradient in the quiescent atmosphere would also broaden the results.

Bibliography

W. Baade and R. Minkowski. On the Indentification of Radio Sources. *Astrophysical Journal*, 119:215, January 1954.

R. D. Blandford and D. G. Payne. Hydromagnetic flows from accretion discs and the production of radio jets. *Monthly Notices of the RAS*, 199:883–903, June 1982.

R. D. Blandford and M. J. Rees. A 'twin-exhaust' model for double radio sources. *Monthly Notices of the RAS*, 169:395–415, December 1974.

A. H. Bridle and R. A. Perley. Extragalactic radio jets. *Annual Review of Astronomy and Astrophysics*, 22(1):319–358, 1984.

D. A. Clarke. A Consistent Method of Characteristics for Multidimensional Magnetohydrodynamics. *Astrophysical Journal*, 457:291, January 1996.

D. A. Clarke. On the Reliability of ZEUS-3D. *Astrophysical Journal, Supplement*, 187:119–134, March 2010.

D. A. Clarke, M. L. Norman, and J. O. Burns. Numerical simulations of a magnetically confined jet. *Astrophysical Journal, Letters*, 311:L63–L67, December 1986.

H. D. Curtis. Descriptions of 762 Nebulae and Clusters Photographed with the Crossley Reflector. *Publications of Lick Observatory*, 13:9–42, 1918.

J. Dennett-Thorpe, A. H. Bridle, P. A. G. Scheuer, R. A. Laing, and J. P. Leahy. Asymmetry of jets, lobe length and spectral index in quasars. *Monthly Notices of the RAS*, 289:753–765, August 1997.

C. R. Evans and J. F. Hawley. Simulation of magnetohydrodynamic flows - A constrained transport method. *Astrophysical Journal*, 332:659–677, September 1988.

B. L. Fanaroff and J. M. Riley. The morphology of extragalactic radio sources of high and low luminosity. *Monthly Notices of the RAS*, 167:31P–36P, May 1974.

A. R. Foley and R. J. Davis. MERLIN radio observations of the quasar 3C 273. *Monthly Notices of the RAS*, 216:679–690, October 1985.

S. T. Garrington, J. P. Leahy, R. G. Conway, and R. A. Laing. A systematic asymmetry in the polarization properties of double radio sources with one jet. *Nature*, 331:147–149, January 1988.

P. E. Hardee, T. Koupelis, M. L. Norman, and D. A. Clarke. Atmospheric gradients and the stability of expanding jets. *Astrophysical Journal*, 373:8–22, May 1991.

D. C. Hines, J. A. Eilek, and F. N. Owen. Filaments in the radio lobes of M87. *Astrophysical Journal*, 347:713–726, December 1989.

R. M. Hjellming. *An Introduction to the NRAO Very Large Array*. National Radio Astronomy Observatory, 1983.

D. C. Homan, R. Ojha, J. F. C. Wardle, D. H. Roberts, M. F. Aller, H. D. Aller, and P. A. Hughes. Parsec-Scale Blazar Monitoring: Proper Motions. *Astrophysical Journal*, 549:840–861, March 2001.

J. S. Hooda and P. J. Wiita. Three-Dimensional Simulations of Jets Crossing Angled Interfaces. In P. E. Hardee, A. H. Bridle, and J. A. Zensus, editors, *Energy Transport in Radio Galaxies and Quasars*, volume 100 of *Astronomical Society of the Pacific Conference Series*, page 377, 1996.

T. Hovatta, M. L. Lister, M. F. Aller, H. D. Aller, D. C. Homan, Y. Y. Kovalev, A. B. Pushkarev, and T. Savolainen. MOJAVE: Monitoring of Jets in Active Galactic Nuclei with VLBA Experiments. VIII. Faraday Rotation in Parsec-scale AGN Jets. *Astronomical Journal*, 144:105, October 2012.

T. Hovatta, E. Valtaoja, M. Tornikoski, and A. Lähteenmäki. Doppler factors, Lorentz factors and viewing angles for quasars, BL Lacertae objects and radio galaxies. *Astronomy and Astrophysics*, 494:527–537, February 2009.

S. Koide, J.-I. Sakai, K.-I. Nishikawa, and R. L. Mutel. Numerical Simulation of Bent Jets: Propagation Into an Oblique Magnetic Field. In P. E. Hardee, A. H. Bridle, and J. A. Zensus, editors, *Energy Transport in Radio Galaxies and Quasars*, volume 100 of *Astronomical Society of the Pacific Conference Series*, page 371, 1996.

A. Lähteenmäki, E. Valtaoja, and K. Wiik. Total Flux Density Variations in Extragalactic Radio Sources. II. Determining the Limiting Brightness Temperature for Synchrotron Sources. *Astrophysical Journal*, 511:112–117, January 1999.

R. A. Laing. The sidedness of jets and depolarization in powerful extragalactic radio sources. *Nature*, 331:149–151, January 1988.

J. P. Leahy and R. A. Perley. VLA images of 23 extragalactic radio sources. *Astronomical Journal*, 102:537–561, August 1991.

R. Liu and G. Pooley. Spectral index and depolarization asymmetry in powerful radio sources. *Monthly Notices of the RAS*, 249:343–351, March 1991.

N. R. MacDonald. Bridging the Gap: Synthetic Radio Observations of Numerical Simulations of Extragalactic Jets. Master's thesis, Saint Mary's University, Halifax, Nova Scotia, August 2008.

D. L. Meier. A Magnetically Switched, Rotating Black Hole Model for the Production of Extragalactic Radio Jets and the Fanaroff and Riley Class Division. *Astrophysical Journal*, 522:753–766, September 1999.

D. L. Meier, S. Edgington, P. Godon, D. G. Payne, and K. R. Lind. A magnetic switch that determines the speed of astrophysical jets. *Nature*, 388:350–352, July 1997.

E. Middelberg, A. T. Deller, R. P. Norris, S. Fotopoulou, M. Salvato, J. S. Morgan, W. Brisken, D. Lutz, and E. Rovilos. Mosaiced wide-field VLBI observations of the Lockman Hole/XMM. *Astronomy and Astrophysics*, 551:A97, March 2013.

L. M. Mullin, J. M. Riley, and M. J. Hardcastle. Observed properties of FRII quasars and radio galaxies at z <1.0. *Monthly Notices of the RAS*, 390:595–621, October 2008.

M. L. Norman. Fluid dynamics of astrophysical jets. *Annals of the New York Academy of Sciences*, 617:217–233, December 1990.

M. L. Norman, K.-H. A. Winkler, L. Smarr, and M. D. Smith. Structure and dynamics of supersonic jets. *Astronomy and Astrophysics*, 113:285–302, September 1982.

C. P. O'Dea and F. N. Owen. Multifrequency VLA observations of the prototypical narrow-angle tail radio source NGC 1265. *Astrophysical Journal*, 301:841–859, February 1986.

R. Ouyed and R. E. Pudritz. Numerical Simulations of Astrophysical Jets from Keplerian Disks. I. Stationary Models. *Astrophysical Journal*, 482:712, June 1997.

J. P. Ramsey and D. A. Clarke. Simulating Protostellar Jets Simultaneously at Launching and Observational Scales. *Astrophysical Journal, Letters*, 728:L11, February 2011.

A. C. S. Readhead. Equipartition brightness temperature and the inverse Compton catastrophe. *Astrophysical Journal*, 426:51–59, May 1994.

P. A. G. Scheuer. Tests of beaming models. In J. A. Zensus and T. J. Pearson, editors, *Superluminal Radio Sources*, pages 104–113, 1987.

M. Seymour. A Numerical Study of Asymmetric Double Radio Sources, April 1997.

W. Steffen, A. J. Holloway, A. Pedlar, and D. J. Axon. IRAS 042 10+0400: Jets Crossing an ISM/IGM Interface? In P. E. Hardee, A. H. Bridle, and J. A. Zensus, editors, *Energy Transport in Radio Galaxies and Quasars*, volume 100 of *Astronomical Society of the Pacific Conference Series*, page 365, 1996.

S. J. Tingay, D. L. Jauncey, J. E. Reynolds, A. K. Tzioumis, E. A. King, R. A. Preston, D. L. Jones, D. W. Murphy, D. L. Meier, T. D. van Ommen, P. M. McCulloch, S. P. Ellingsen, M. E. Costa, P. G. Edwards, J. E. J. Lovell, G. D. Nicolson, J. F. H. Quick, A. J. Kemball, V. Migenes, P. Harbison, P. A. Jones, G. L. White, R. G. Gough, R. H. Ferris, M. W. Sinclair, and R. W. Clay. The Subparsec-Scale Structure and Evolution of Centaurus A: The Nearest Active Radio Galaxy. *Astronomical Journal*, 115:960–974, March 1998.

G. V. Ustyugova, A. V. Koldoba, M. M. Romanova, V. M. Chechetkin, and R. V. E. Lovelace. Magnetohydrodynamic simulations of outflows from accretion disks. *Astrophysical Journal, Letters*, 439:L39–L42, February 1995.

R. C. Vermeulen. Superluminals: When Have We Seen Them All? In P. E. Hardee, A. H. Bridle, and J. A. Zensus, editors, *Energy Transport in Radio Galaxies and Quasars*, volume 100 of *Astronomical Society of the Pacific Conference Series*, page 117, 1996.